

Effective temperature concept evaluated in an active colloid mixture

Ming Han^{a,1}, Jing Yan^{b,1}, Steve Granick^{c,2}, and Erik Luijten^{d,e,f,2}

^aApplied Physics Graduate Program, Northwestern University, Evanston, IL 60208; ^bDepartment of Materials Science and Engineering, University of Illinois, Urbana, IL 61801; ^cInstitute for Basic Science Center for Soft and Living Matter, Ulsan National Institute of Science and Technology, Ulsan 689-798, South Korea; ^dDepartment of Materials Science and Engineering, Northwestern University, Evanston, IL 60208; ^eDepartment of Engineering Sciences and Applied Mathematics, Northwestern University, Evanston, IL 60208; and ^fDepartment of Physics and Astronomy, Northwestern University, Evanston, IL 60208

Contributed by Steve Granick, June 11, 2017 (sent for review April 24, 2017; reviewed by Denis Bartolo and Angelo Cacciuto)

Thermal energy agitates all matter, and its competition with ordering tendencies is a fundamental organizing principle in the physical world; this observation suggests that an effective temperature might emerge when external energy input enhances agitation. However, despite the repeated proposal of this concept based on kinetics for various nonequilibrium systems, the value of an effective temperature as a thermodynamic control parameter has been unclear. Here, we introduce a two-component system of driven Janus colloids, such that collisions induced by external energy sources agitate the system, and we demonstrate quantitative agreement with hallmarks of statistical thermodynamics for binary phase behavior: the archetypal phase diagram with equilibrium critical exponents, Gaussian displacement distributions, and even capillarity. The significance is to demonstrate a class of dynamical conditions under which thermodynamic analysis extends quantitatively to systems that are decidedly nonequilibrium except that the effective temperature differs from the physical temperature.

active matter | colloid | temperature | thermodynamics | nonequilibrium

The tug of war between randomization due to temperature and ordering from enthalpy governs whether components mix or demix at equilibrium. The even larger realm of nonequilibrium systems similarly shows empirically that particles with different dynamic modes may segregate spontaneously. Examples include bacteria (1), granular particles under shaking (2), and active colloids (3). This concept has inspired various efforts (4, 5) to extend the profound insights of statistical thermodynamics to nonequilibrium systems. In particular, the concept of defining an effective temperature based upon the kinetics of a system has repeatedly been proposed for synthetic active materials (6, 7), biological motors (8–10), granular materials (11–13), and turbulent fluids (14). However, the predictive value of this effective temperature has been explored only to a limited extent (15, 16). Here, without wishing to minimize important differences between specific nonequilibrium phenomena, we test the concept that some of them may be indeed governed by an emergent effective temperature.

Results

Experimentally, we apply external electric and magnetic fields (Fig. 1A) to Janus silica spheres with a diameter of 3 μm , one hemisphere coated with a thin Ni/Ti cap and an SiO₂ protective layer to render their outermost chemical makeup homogeneous. The particles settle to the bottom of the planar sample cell to form a quasi-two-dimensional (quasi-2D) system, but, as they remain dispersed in water, we avoid complications of solid–solid friction (17) often encountered in granular systems. The ac electric field applied perpendicular to the monolayer causes the particles to orient their equators vertically and self-propel (“swim”) with their nonmetallic hemisphere facing forward (18), while a magnetic field, rotating at low frequency in the plane, forces swimming particles to trace circular orbits with a tunable radius R (Movie S1). Spontaneous symmetry breaking

results. The Janus colloids dynamically differentiate into two types that orbit 180 degrees out of phase, with their nonmetallic sides facing in opposite directions. Particles that are in phase never collide, whereas those that orbit out of phase have opportunities to collide with each other when close by (Fig. 1B). Brownian dynamics computer simulations, matching the experimental conditions in their essential respects, extend the experiments to otherwise inaccessible regimes. In these simulations, particles carrying an electric dipole moment are confined within a 2D plane, and experience a swimming force directed from the metal toward the silica hemisphere. The effect of the rotating magnetic field is modeled as an external torque driving the circular motion of each particle. Without this rotation, oppositely swimming particles would separate into lanes to reduce collisions, a known phenomenon (19). However, at finite R , lanes grow only to a finite length (Fig. S1) as they continually break and reform to follow the orbits (Movie S2). Viscous drag dissipates the injected energy, and the collisions disturbing the intrinsic circular orbits cause particle trajectories to fluctuate.

Hallmarks of classical Brownian motion are observed when we study the long-time behavior of particle dynamics by inspecting their positions once per rotation cycle (“stroboscopic” view), at symmetric (50:50) composition. First, the mean squared displacements are proportional to the number of cycles (Fig. 1C). Second, displacements trace a Gaussian distribution over three orders of magnitude of probability density that were inspected (Fig. 1D). The Gaussian distribution was further confirmed by

Significance

In the long-standing debate on whether the insights of statistical thermodynamics could apply to nonequilibrium systems, a key unsolved problem is whether it is useful to postulate an emergent effective temperature, different from the thermal temperature. Here, we introduce a two-component system of driven Janus colloids such that collisions induced by external energy sources play the role of temperature. We find that this nonequilibrium system quantitatively behaves as if at equilibrium, with collisions caused by differential rhythmic motion between the two components acting as a strict analog to thermal motion. We demonstrate that the effective temperature can serve as a common control parameter for both kinetics and phase behavior.

Author contributions: J.Y., S.G., and E.L. designed research; M.H. and J.Y. performed research; M.H., J.Y., S.G., and E.L. analyzed data; and M.H., J.Y., S.G., and E.L. wrote the paper.

Reviewers: D.B., Ecole Normale Supérieure de Lyon; and A.C., Columbia University.

The authors declare no conflict of interest.

Freely available online through the PNAS open access option.

¹M.H. and J.Y. contributed equally to this work.

²To whom correspondence may be addressed. Email: sgranick@ibs.re.kr or luijten@northwestern.edu.

This article contains supporting information online at www.pnas.org/lookup/suppl/doi:10.1073/pnas.1706702114/-DCSupplemental.

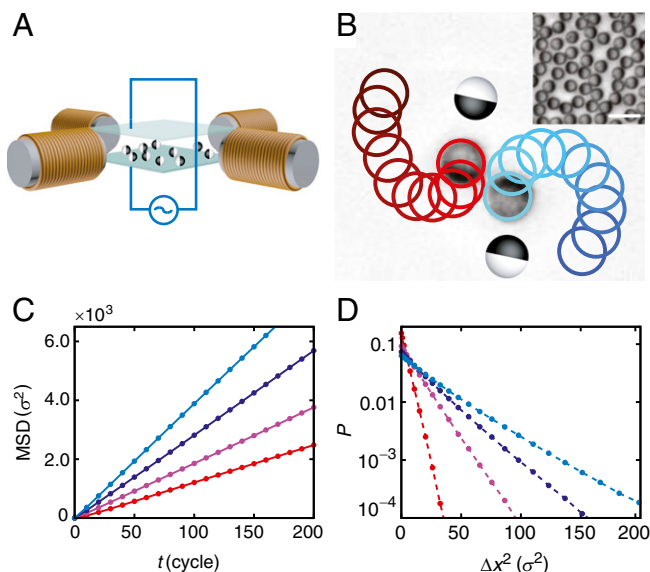


Fig. 1. Emergent Brownian motion. (A) Sketch of the experimental setup. A vertical ac electric field and a planar rotating magnetic field are applied to a monolayer suspension of Janus colloids. (B) Experimental image of a two-particle collision event overlaid with reconstructed trajectories, color-coded with time (varying from dark to bright). (Inset) Experimental image of oppositely moving particles at area fraction 0.44 showing that they align their Janus interfaces with the magnetic field while separating into two species with their nonmetallic hemispheres facing in opposite directions. All particles perform circular motion, in this example with radius $R = 3.52\sigma$ ($\sigma = 3 \mu\text{m}$, the particle diameter). (Scale bar: $10 \mu\text{m}$.) (C) Time evolution of mean squared displacement (MSD). (D) Probability of displacement Δx along the x axis after one rotation cycle. Results in C and D are measured in simulations with $R = 2\sigma$ (red), 4σ (purple), 6σ (violet), and 8σ (blue).

inspection of the kurtosis (Fig. S2). We emphasize that our experiments are consistent with the simulations wherever comparison is possible, whereas the simulations offer better and more exhaustive statistics. Increasing diffusion with R suggests that R plays the role of effective temperature, but it remains to explain why.

Strong claims demand strong evidence. According to the textbook Langevin approach (20) that describes thermal fluctuation dynamics in equilibrium, random forces must satisfy the following requirements: (i) their (time or ensemble) average must vanish; (ii) orthogonal components of the random forces on a particle must be independent; and (iii) each component of the random force must decorrelate instantaneously and have a variance proportional to temperature. This very approach, mathematically equivalent to the Fokker–Planck equation (20), is used widely in molecular dynamics simulations to control temperature. We tested these points in simulations. Condition i is satisfied by symmetry of the circular motion. In this overdamped system, random forces originate from interparticle collisions, but are immediately balanced by the viscous forces and manifest themselves as perturbations around the circular orbits. Satisfying conditions ii and iii, orthogonal components of the perturbations tangential and normal to the circular orbit are independent, and both decorrelate at short times, within one tenth of a cycle, as shown in Fig. 2.

The resulting Smoluchowski equation (21) explains the emergence of Brownian motion. Consistently, the diffusivity D measured on long time scales and its value computed from the autocorrelation function of the perturbations agree quantitatively (Fig. 2C). Furthermore, the Gaussian displacement distribution that we observe is also explained, as the Smoluchowski equation yields such a distribution with variance determined by

the variance of the random forces, regardless of whether these forces are Gaussian random variables (20) (Fig. 2A). The rapid decorrelation of the random forces (condition iii above; Fig. 2B) guarantees Markovian dynamics in the stroboscopic view. In combination with the steady-state nature of the system, this Markovian dynamics implies that the fluctuation–dissipation theorem applies even out of equilibrium (9). According to the Einstein relation, D is proportional to absolute temperature. Because we find that, in our system, D is linear with the radius R (Fig. 2C), it is physically meaningful to represent and control the effective temperature by the radius. Indeed, as the radius increases, more interparticle collisions occur within each cycle, and thus larger randomness is introduced into the system, analogous to increasing the temperature.

Another hallmark of thermodynamics is phase separation, as illustrated in Fig. 3. Investigating this, we note that phase separation between the two dynamical species arises because collisions between these particles of different types lead to effective attraction between particles of the same type. Despite the absence of enthalpy of interaction, there is a tendency to aggregate, akin to the concept of osmotic pressure. To quantify this, we extract the potential of mean force (22, 23) V_{PMF} from the radial distribution functions $g(r)$ of the two species (Fig. 3B). This procedure yields the pair potential in the intrinsic “thermal” energy unit, even though, here, that is not $k_{\text{B}}T$. The fact that attraction strengthens with decreasing R suggests that phase segregation might ensue. Indeed, we observe this (Fig. 3A and Movie S3) experimentally.

The development of equilibrium statistical thermodynamics was revolutionized when it succeeded to explain the critical point with the concomitant universal singular behavior (24), so now we likewise apply this stringent test to the nonequilibrium dynamical system introduced here. Symmetry dictates that this point must occur in a system with equal numbers of A and B particles. When R is decreased to a critical value $R_{\text{c}} = 1.84\sigma$ at area fraction 0.37 in the simulations (between σ and 2σ in experiment, depending on particle density), the spatial distribution of the local order parameter $s = \phi_{\text{A}} - \phi_{\text{B}}$ (ϕ is the composition fraction) shows self-similar patterns indicating a diverging correlation length, the hallmark of criticality (Fig. 4A and Movie S4).

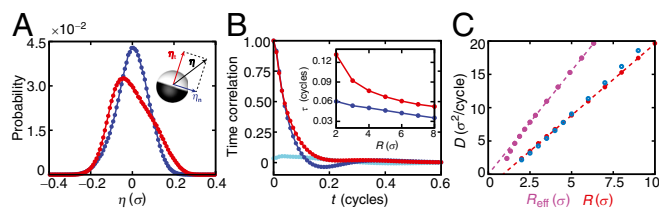


Fig. 2. Statistics of collision-induced perturbations and effective temperature in simulation. Particle displacements Δx in the particle rotation reference frame with time interval $\Delta t = 0.01$ cycles are tabulated and decomposed into the average $\langle \Delta x \rangle$ due to their circular orbit and the remaining fluctuations η that correspond to random perturbations. (A) Probability distributions of perturbations tangential (η_t , red) and normal (η_n , blue) to orbits at $R = 4\sigma$. Both η_t and η_n are non-Gaussian random variables with vanishing averages. (Inset) Decomposition of perturbation η . (B) Autocorrelation functions of η_t and η_n and their cross-correlation function (cyan). The η_t and η_n quickly decorrelate with themselves, and are also nearly independent at all times. (Inset) Dependence of relaxation time τ on R for η_t and η_n . (C) Dependence of diffusivity D on R . Direct measurement and prediction based on the autocorrelation functions of perturbations $D = \sum_{i=0}^{\infty} [\eta_t(0) \cdot \eta_t(i\Delta t) + \eta_n(0) \cdot \eta_n(i\Delta t)] \cdot \cos(i\omega\Delta t) \cdot \Delta t$, where $\cos(i\omega\Delta t)$ is the curvature correction caused by the circular motion, are shown as red and blue circles, respectively. The dependence is evaluated with respect to both the apparent radius R (red) as determined only by the rotating magnetic field and the actual radius R_{eff} (purple) modulated by particle collisions.

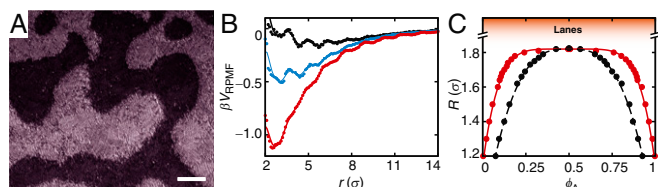


Fig. 3. Phase separation. (A) Experimental image at $R = 0.88\sigma$, area fraction 0.45, and $\phi_A = 0.5$. (Scale bar: $60\ \mu\text{m}$.) (B) Relative potential of mean force V_{RPMF} at $R = 1.5\sigma$ (red), 3σ (blue) and 4.5σ (black). (C) Phase diagram from simulations. Binodal and spinodal curves are shown in red and black, respectively.

Consistently, we find that the susceptibility χ , the variance of the local order parameter s , also diverges around R_c in the limit of large system size (Fig. 4B). Applying finite-size scaling (25), we find that the measured susceptibility maximum χ_{max} diverges as a function of linear system size L (Fig. 2C, *Inset*) with exponent 1.71 ± 0.05 , agreeing with the 2D Ising critical exponent ratio $\gamma/\nu = 7/4$ for an equilibrium system with scalar order parameter and short-range interactions. Moreover, as shown in Fig. 4C, the global order parameter exhibits singular behavior $M \approx |R - R_c|^\beta$ with $\beta = 0.127 \pm 0.003$, again consistent with the pertinent equilibrium prediction $1/8$. This agreement with expectations for equilibrium critical phenomena extends beyond static properties, encompassing even dynamics: The relaxation time of the system diverges as $(R - R_c)^{-z\nu}$ upon approaching the critical point from the supercritical regime (Fig. 4D), with $z\nu = 3.7 \pm 0.1$, in agreement with $z\nu = 4 - \eta = 3.75$ for a conserved order parameter (26). The discovery of these highly nontrivial (24) power laws shows that the dynamical system quantitatively reflects all

universal aspects of a continuous phase transition, including a consistent and complete set of critical exponents belonging to this known equilibrium universality class. We conjecture that a similar framework may apply to other steady-state nonequilibrium systems also, provided that the reasoning leading to designing this experimental system is satisfied, as, in an equilibrium system, all of these findings can be derived from a free-energy functional (25, 26). Although no quantitative derivation can be presented at this time, to discover this hint of such a functional in a nonequilibrium system is stimulating.

Furthermore, mapping a complete “phase diagram” parameterized by R and ϕ_A , Fig. 3C visually and quantitatively resembles the established phase diagram of binary fluids, sectioned by a binodal and a spinodal curve. Validating the simulations, experiments within the phase boundary display the expected interconnected patterns known as spinodal decomposition (Fig. 3A and *Movie S5*) at the critical composition, and nucleation-and-growth behavior (*Movie S6*) at off-critical compositions close to the phase boundary. At the initial stage when (in the case of thermal phase separation) most differences between these behaviors are expected, the differences here too are clear (Fig. 5A): Whereas the former displays patterns with a specific wavelength, the latter relies on random excitations to form a nucleus and hence lacks a characteristic length scale. Nascent nuclei fluctuate wildly, then merge and grow into spherical domains with time (*Movies S6* and *S7*). Late-stage coarsening behavior of the spinodal pattern is also consistent with the equilibrium concept of surface tension driving domain growth with a power law exponent of 0.5 (Fig. 5B–D and Fig. S3). The existence of an effective surface tension can be clearly seen from the spreading of a spherical droplet onto a larger domain

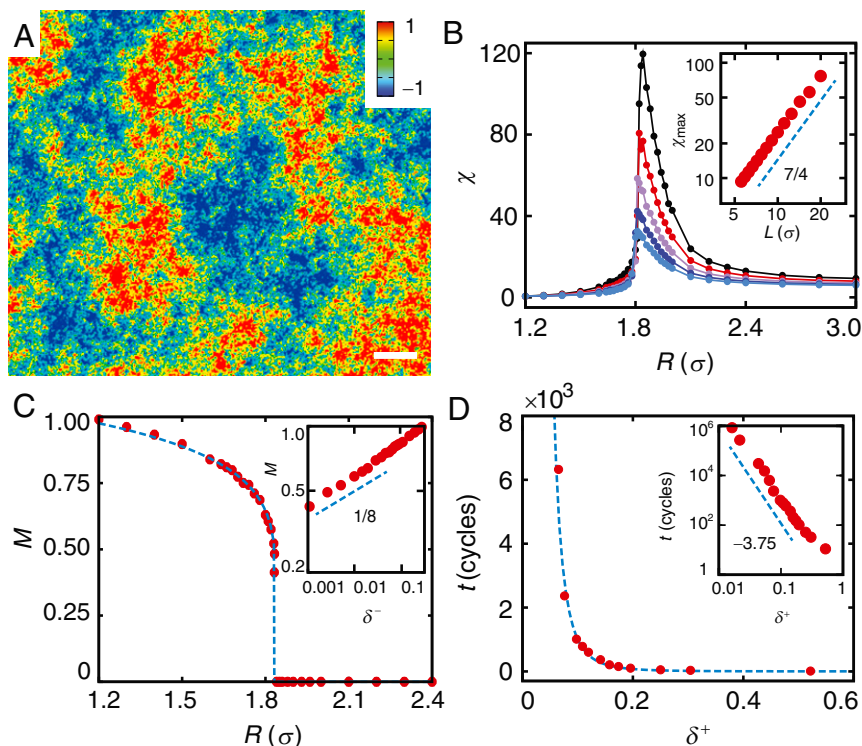


Fig. 4. Critical phenomena in simulation. (A) Spatial distribution of the local order parameter s in simulation for a symmetric mixture at the critical point $R_c = 1.84\sigma$. (Scale bar: 120σ .) (B) Dependence of susceptibility χ measuring the composition fluctuations on R , evaluated for subcells of different side lengths $L = 16.67\sigma$ (black), 12.5σ (red), 10σ (purple), 8.33σ (navy), and 7.14σ (blue). (*Inset*) Relation between maximum susceptibility χ_{max} and subcell size L , plotted on a logarithmic scale. The blue line represents the 2D Ising power law $7/4$. (C) Dependence of the global order parameter M on R . (*Inset*) M versus $\delta^- = (R_c - R)/R_c$ (for $R < R_c$) on a logarithmic scale. The blue line has a power-law exponent $1/8$. (D) Correlation time of the entire system as a function of $\delta^+ = (R - R_c)/R_c$. *Inset* employs a log–log scale. The blue curve has the universal power-law exponent $-15/4$.

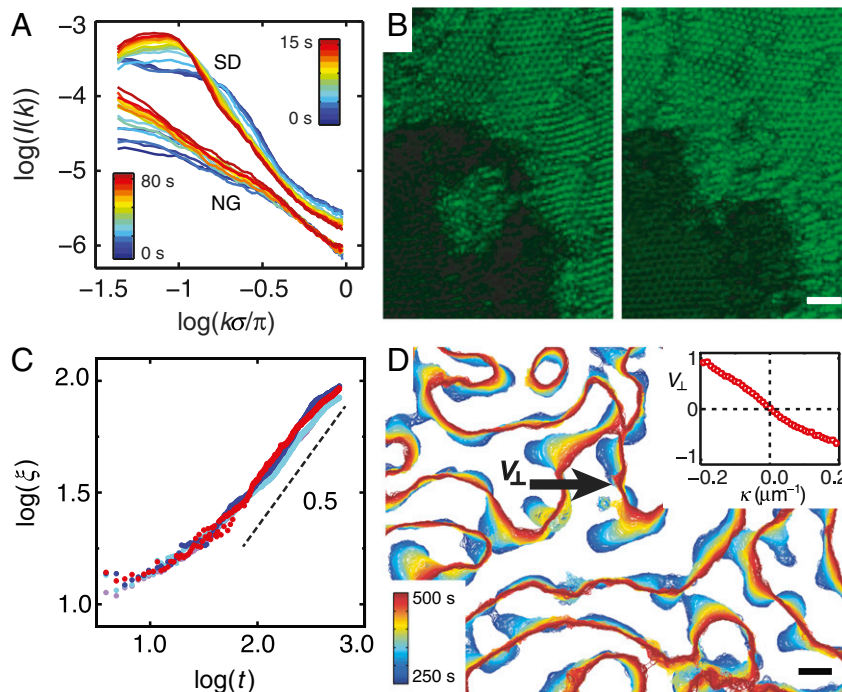


Fig. 5. Dynamics of phase segregation and coarsening in experiment. (A) Time evolution of the scattering function $I(k)$ at initial states for a system undergoing spinodal decomposition (SD; $\phi_A = 0.5$, $R = 0.88\sigma$) as well as a system exhibiting nucleation and growth (NG; $\phi_A = 0.15$, $R = 0.5\sigma$). (B) Sequential experimental images showing a spreading process. Time difference: 42 s. (Scale bar: 20 μm .) (C) Time evolution of the correlation length ξ . Four independent samples are shown. (D) Time evolution of domain boundaries. (Inset) Normal component of boundary velocity v_{\perp} as marked in D, plotted with respect to local curvature κ . Unit is micrometers per second. (Scale bar: 50 μm .)

(Fig. 5B and Movie S8). However, the capillary velocity (Fig. 5D, Inset) is seven orders of magnitude less than that of water in which these colloidal suspensions are immersed. Spinodal patterns at the critical composition, and nucleation patterns off the critical composition, present another pleasing analogy to equilibrium mixtures.

Discussion

In conclusion, by designing this two-component system of driven Janus colloids, we have demonstrated the possibility of a nearly complete mapping between nonequilibrium phenomena and thermodynamics. Here, constant collisions powered by external fields play a role similar to that of thermal agitations, controlling both kinetics and steady states of the system. Akin to random forces in the Langevin approach, they cause the particles to diffuse at large time scales and display the fluctuation–dissipation relation. The diffusivity D measured from this long-term kinetics precisely matches the prediction based upon the short-term fluctuations (Fig. 2C). The linear dependence of D on the radius R of particle rotation further suggests that this radius plays the role of an effective temperature T , controlling the randomness of the system. More importantly, the effective temperature consistently governs the steady states: As R (or T) is decreased, the system undergoes a transition from a mixture to segregated domains similar to a thermal binary fluid, even with an archetypal phase diagram and 2D Ising critical exponents. This temperature dependence is different from that of the motility-induced phase behavior found in systems of linearly self-propelled particles (16, 27). There, with the ideal single-particle diffusivity D_0 defined as effective temperature T , phase separation occurs as D_0 (or T) is increased, the opposite of conventional thermal systems; this is because the diffusion of linearly self-propelled particles is primarily a combination of rotational fluctuations and particle motility. The motility neither introduces nor distributes randomness

among the particles, making the diffusivity D_0 an improper measure of the effective temperature. Recent work suggests that, instead, the motility gives rise to an effective pressure that causes particle aggregation (7). In contrast, in our system, randomness is induced solely by interparticle collisions and, in the one-phase regime, can be shared among particles, making it possible to define a universal effective temperature that governs both kinetics and phase behavior.

A devil’s advocate might argue that there is no need to go beyond the diffusivity D to define a temperature, as the Fokker–Planck or Smoluchowski equation that describes the microstructure in the suspension is completely specified by diffusivity and interparticle forces. However, we consider that defining an emergent temperature by the imposed radius of rotation R offers deeper understanding by connecting to the mature framework of statistical thermodynamics and enabling the thermodynamics-based predictions that our simulations and experiments validate. Furthermore, because no noise is introduced in our simulations, the effective temperature is not an arbitrary simulation input but instead emerges naturally from particle collisions.

We note limitations of the effective temperature concept based upon interparticle collisions. First, the concept depends on particle dynamics, so that particles moving at different radii do not share the same temperature. Second, the temperature also varies with local environment once phase separation sets in. Then, the effective temperature locally drops to zero and these systems crystallize (Movies S6–S8), unlike equilibrium systems where temperature is inherently uniform. This nonuniform temperature distribution has been also reported in other non-equilibrium systems (23, 27). Third, this effective temperature is only valid on long time scales, and is not necessarily reflected in instantaneous particle arrangements and kinetics. For instance, the mixed state at high effective temperature consists of lanes (Movie S2), unlike an equilibrium system. Moreover, during

coarsening, collisions at the domain boundary drive particles to move in opposite directions parallel to the boundary (Fig. 6). Particle currents along domain boundaries were also reported in a recent work on the phase separation of oppositely spinning particles (23), but there the role of effective temperature was not discussed. The findings in this paper should generalize naturally to other dynamic components that perform three-dimensional periodic or chaotic motion that traces back to the origin with statistically significant numbers of collisions. However, these limitations underscore that care is needed to apply the effective temperature concept despite the nontrivial predictive capability demonstrated here.

Materials and Methods

Particle Synthesis. Onto a planar submonolayer of monodisperse 3- μm silica particles (Tokuyama), obtained by drying 20 μL of 2 wt% particle suspension in deionized (DI) water onto a half glass slide (1.5 inch \times 1 inch), a thin film of 4-nm Ni/10-nm Ti/5-nm SiO_2 is sequentially deposited vertically using electron beam deposition in vacuum. The monolayer is washed thoroughly with DI water and isopropyl alcohol, and then sonicated in 20 mL of DI water to collect the particles in a 50-mL centrifuge tube.

Setup. A spatially homogeneous rotating magnetic field is generated by two orthogonal pairs of solenoids as described previously (28). Briefly, the two pairs of solenoids receive two sinusoidal voltages from a function generator, amplified by power amplifiers, with $\pi/2$ phase difference between each signal to produce an in-plane rotating field B .

The electric field is applied by sandwiching the particles between two coverslips coated with indium tin oxide (ITO) from SPI Supplies (29). The ITO-coated coverslips are further coated with 25 nm of SiO_2 using electron beam deposition to electrostatically prevent the particles from surface adsorption. A thin strip on one side of the ITO-coated coverslip is left uncoated during the SiO_2 deposition, and is used later to connect to a function generator (Agilent 33522A) via copper tapes. A square wave of 5 kHz and 7 V is used for all experiments. The two ITO-coated coverslips are separated by a spacer (SecureSeal; Grace Biolab) about 120 μm thick, with a 9-mm-diameter hole.

Movies are taken in a customized microscope using an LED light source (MCWHL2; Thorlabs) and a CMOS camera (5012M GigE; Edmund Optics). For a high-magnification view in which the Janus features can be resolved, a 50 \times long-working-distance objective (numerical aperture 0.55; Mitutoyo) is used. For large-

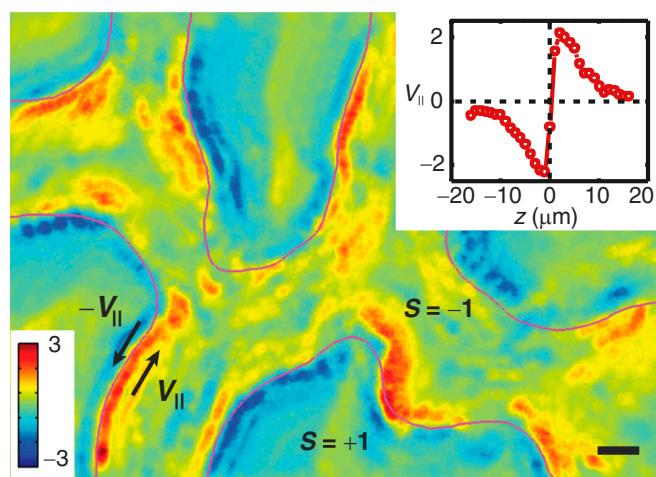


Fig. 6. Particle velocity distribution at $R = 0.54\sigma$ and $\phi_A = 0.5$ in experiment. A heat map is shown of the velocity $V_{||}$, defined as particle velocity parallel to the nearby domain boundary and averaged over 5 s during which the domain boundary barely changes. Unit is micrometers per second. (Scale bar: 10 μm .) Due to collisions, particles on the two sides of a domain boundary move in opposite directions. (Inset) Dependence of $V_{||}$ on the distance z to the domain boundary. Away from the boundary, $V_{||}$ first displays a linear decay, akin to a standard viscous response. Therefore, one can conceptually think of the two colliding domains as shearing each other. Toward the interior of the domain, the velocity levels off, consistent with the observed crystallization.

scale views, a 10 \times long-working-distance objective (numerical aperture 0.28; Mitutoyo) is used. In this case, it is not possible to differentiate the silica/metal sides of each individual sphere. Instead, we use “tilted illumination” and shine light on the particle from an oblique angle, so that a particle appears dark or bright depending on whether the metal side is facing toward or away from the light source. We then use stroboscopic sampling, only analyzing one frame per cycle, such that one species is consistently brighter than the other. When we zoom in to take a magnified view of the system, the optics is well aligned, allowing us to clearly differentiate between the metal-coated and the silica hemisphere.

Experimental Procedure. Ten microliters of concentrated particle suspension is dropped onto an ITO-coated coverslip with spacer, and then sandwiched with another ITO coverslip. This procedure produces a monolayer of colloids with area fraction between 0.35 and 0.45. Repeated experiments can be done on one sample for 2 to 3 h, after which significant particle clustering or substrate adsorption occurs. Before each run, a constant DC magnetic field is applied in the image plane to cause particles to assemble into zigzag chains, which ensures a completely mixed initial state without memory of earlier states. A rotating magnetic field is then applied with a strength of 5 mT and a frequency ranging from 16 Hz to 0.05 Hz, followed immediately by an ac electric field (5 kHz, 58 V/mm); this we define as $t = 0$ s. Movies are taken up to 20 min for each condition, at a rate of 16 frames per second.

To change the ratio between the two species, a pulse of additional z-axis magnetic field is applied. Although the precise mechanism of the conversion is unclear, we are able to roughly control the composition by varying the strength and duration of this z field.

Image Processing for Large View. We first subtract the background light gradient due to the intentional optical misalignment, obtained by averaging over a whole movie. The image is then smoothed and binarized, with each pixel now having a local order parameter $s(r)$ (defined in *Analysis of Phase Transition*) of value +1 or -1. Spatial correlation $C(r)$, defined as $\langle s(0) \cdot s(r) \rangle$, is calculated from the binarized image. Correlation length ξ is defined as the r value where $C(r)$ first passes zero. Linear interpolation between the last positive value and first negative value is used to improve accuracy. Structure factor is obtained by applying fast Fourier transform to the image and taking a radial average.

Simulation Procedure. We model this overdamped and fully driven quasi-2D system via athermal Brownian dynamics simulations. Confined to the x - y plane, Janus particles of diameter $\sigma = 3 \mu\text{m}$ with area fraction 0.37 (to match the experiment) move in a square, periodic domain of side length 200σ . Their positions $\mathbf{r}(t)$ and orientations $\Omega(t)$ follow the master equations

$$\begin{cases} \dot{\mathbf{r}}(t) = \mathbf{F}/\zeta_t \\ \dot{\Omega}(t) = \mathbf{T} \times \Omega/\zeta_r \end{cases}$$

where \mathbf{F} and \mathbf{T} are, respectively, the force and the torque exerted on the particle, and ζ_t and ζ_r refer to the translational and rotational drag coefficients. Here reduced units are used, with the particle mass $m = 3.74 \times 10^{-14}$ kg as mass unit, the particle diameter σ as length unit, and $\tau = 10^{-3}$ s as time unit. Given the dynamic viscosity μ of the water, those spherical particles have $\zeta_t = 3\pi\mu\sigma = 672.8$ and $\zeta_r = \pi\mu\sigma^3 = 224.3$. According to the reciprocal theory (30), the action of the electric and magnetic fields in experiment can be modeled as a driven circular motion caused by an external force $F_{\text{ex}} = \zeta_t v = 4.7$ (with $v \approx 21 \mu\text{m/s}$ as the measured terminal swimming velocity) and an external torque $T_{\text{ex}} = \zeta_r \omega$ (with ω as the tunable angular frequency). Two types of particles are considered, with oppositely directed driving forces at each instant.

In addition to the external driving, interactions between the particles also affect their motions. Excluded-volume effects are implemented as shifted-truncated Lennard-Jones interactions with $\sigma_{\text{L}} = 1$, $\epsilon_{\text{L}} = 1$, and cutoff at $r_c = 2^{1/6}$. In experiment, due to the z-directional electric field, the particles experience an induced dipolar force, which is isotropic in the x - y plane and decays as $A \cdot r^{-4}$. Here we set the strength $A = 7.5$ so that the dipolar interaction balances the driving force at r_c . Note that this is a simplified version of our previous model (29), where both sides of a Janus sphere carry an induced electric dipole shifted away from the particle center, and the resultant off-centered dipolar interaction can reorient the particle. In the current system, the magnetic field applied to control particle orientation overwhelms this interaction-induced reorientation mechanism. Therefore, we only consider the overall induced electric dipole moment on each particle and the resultant soft repulsion between particles.

All simulations start with a random configuration and proceed for at least 10^9 steps with time step $dt = \tau$. This duration corresponds to around 10^5

rotation cycles (equivalent to 50 h in experiment), which we found to be sufficient for the system to reach a steady state.

Analysis of Phase Transition. To quantify the phase transition, we define the order parameter as the composition difference $s = \phi_A - \phi_B$, which is conserved globally but fluctuates locally in the system. Here we divide the entire system into relatively small subcells of side length $L = 12.5\sigma$ and record their composition fluctuations, which mimic those present in the grand canonical ensemble. The histogram yields the order-parameter distribution, which changes from a Gaussian distribution centered at 0 to a symmetric bimodal distribution as R decreases at symmetric composition (Fig. S4). The peak position denotes the global order parameter M of the system, specifically,

$$M = \begin{cases} s_{\text{peak}}, & \text{single peak } s_{\text{peak}} \\ \left(|s_{\text{peak}}^-| + |s_{\text{peak}}^+| \right) / 2, & \text{two peaks } s_{\text{peak}}^- \text{ and } s_{\text{peak}}^+ \end{cases}$$

It displays singular behavior at the transition point R_c (Fig. 4C). The susceptibility is defined as

$$\chi = \begin{cases} L^2 \langle (s - s_{\text{peak}})^2 \rangle, & \text{single peak } s_{\text{peak}} \\ L^2 \left[\langle (s - s_{\text{peak}}^-)^2 \rangle_{s \leq s_{\text{peak}}^-} + \langle (s - s_{\text{peak}}^+)^2 \rangle_{s > s_{\text{peak}}^+} \right], & \text{two peaks } s_{\text{peak}}^- \text{ and } s_{\text{peak}}^+ \end{cases}$$

To study the divergence of χ , we perform a finite-size scaling analysis by systematically varying the subcell size L from 5.6σ to 20σ and exploring the rise of the maximum susceptibility χ_{max} with L (Fig. 2C).

ACKNOWLEDGMENTS. At the Institute for Basic Science Center for Soft and Living Matter, S.G. acknowledges support by the Institute for Basic Science, project code IBS-R020-D1. This work was supported by the U.S. Department of Energy, Division of Basic Energy Sciences, under Award DE-FG02-07ER46471, through the Frederick Seitz Materials Research Laboratory at the University of Illinois at Urbana-Champaign (to J.Y. and S.G.) and by the National Science Foundation (NSF) under Award Nos. DMR-1121262 and DMR-1610796 (to M.H. and E.L.). We acknowledge support from NSF CBET-0853737 for equipment and from the Quest high-performance computing facility at Northwestern University (to M.H. and E.L.). J.Y. holds a Career Award at the Scientific Interface from the Burroughs Wellcome Fund.

- Klausen M, Aaes-Jørgensen A, Molin S, Tolker-Nielsen T (2003) Involvement of bacterial migration in the development of complex multicellular structures in *Pseudomonas aeruginosa* biofilms. *Mol Microbiol* 50:61–68.
- Möbius ME, Lauderdale BE, Nagel SR, Jaeger HM (2001) Brazil nut effect: Size separation of granular particles. *Nature* 414:270.
- Stenhammar J, Wittkowski R, Marenduzzo D, Cates ME (2015) Activity-induced phase separation and self-assembly in mixtures of active and passive particles. *Phys Rev Lett* 114:018301.
- Cugliandolo LF (2011) The effective temperature. *J Phys A Math Theor* 44:483001.
- Dieterich E, Camunas-Soler J, Ribezzi-Crivellari M, Seifert U, Ritort F (2015) Single-molecule measurement of the effective temperature in non-equilibrium steady states. *Nat Phys* 11:971–977.
- Palacci J, Cottin-Bizonne C, Ybert C, Bocquet L (2010) Sedimentation and effective temperature of active colloidal suspensions. *Phys Rev Lett* 105:088304.
- Takatori SC, Brady JF (2015) Towards a thermodynamics of active matter. *Phys Rev E Stat Nonlin Soft Matter Phys* 91:032117.
- Le Goff L, Amblard F, Furst EM (2002) Motor-driven dynamics in actin-myosin networks. *Phys Rev Lett* 88:018101.
- Prost J, Joanny J-F, Parrondo JMR (2009) Generalized fluctuation-dissipation theorem for steady-state systems. *Phys Rev Lett* 103:090601.
- Wang S, Wolynes PG (2011) On the spontaneous collective motion of active matter. *Proc Natl Acad Sci USA* 108:15184–15189.
- Edwards SF (1993) The role of entropy in the specification of a powder. *Granular Matter: An Interdisciplinary Approach*, ed Mehta A (Springer, New York).
- D’Anna G, Mayor P, Barrat A, Loreto V, Nori F (2003) Observing Brownian motion in vibration-fluidized granular matter. *Nature* 424:909–912.
- Song C, Wang P, Makse HA (2005) Experimental measurement of an effective temperature for jammed granular materials. *Proc Natl Acad Sci USA* 102:2299–2304.
- Cross MC, Hohenberg PC (1993) Pattern formation outside of equilibrium. *Rev Mod Phys* 65:851–1112.
- Bechinger C, et al. (2016) Active particles in complex and crowded environments. *Rev Mod Phys* 88:045006.
- Cates ME, Tailleur J (2015) Motility-induced phase separation. *Annu Rev Condens Matter Phys* 6:219–244.
- Hartley RR, Behringer RP (2003) Logarithmic rate dependence of force networks in sheared granular materials. *Nature* 421:928–931.
- Gangwal S, Cayre OJ, Bazant MZ, Velez OD (2008) Induced-charge electrophoresis of metalodielectric particles. *Phys Rev Lett* 100:058302.
- Vissers T, et al. (2011) Lane formation in driven mixtures of oppositely charged colloids. *Soft Matter* 7:2352–2356.
- Van Kampen NG (2007) *Stochastic Processes in Physics and Chemistry* (North-Holland, Amsterdam), 3rd Ed.
- von Smoluchowski M (1906) Zur kinetischen Theorie der Brownschen Molekularbewegung und der Suspensionen. *Ann Phys* 326:756–780.
- Kirkwood JG (1935) Statistical mechanics of fluid mixtures. *J Chem Phys* 3:300–313.
- Nguyen NHP, Klotsa D, Engel M, Glotzer SC (2014) Emergent collective phenomena in a mixture of hard shapes through active rotation. *Phys Rev Lett* 112:075701.
- Wilson KG (1974) The renormalization group and the ϵ expansion. *Phys Rep* 12: 75–199.
- Fisher ME, Barber MN (1972) Scaling theory for finite-size effects in the critical region. *Phys Rev Lett* 28:1516–1519.
- Hohenberg PC, Halperin BI (1977) Theory of dynamic critical phenomena. *Rev Mod Phys* 49:435–479.
- Fily Y, Marchetti MC (2012) Athermal phase separation of self-propelled particles with no alignment. *Phys Rev Lett* 108:235702.
- Yan J, Bloom M, Bae SC, Luijten E, Granick S (2012) Linking synchronization to self-assembly using magnetic Janus colloids. *Nature* 491:578–581.
- Yan J, et al. (2016) Reconfiguring active particles by electrostatic imbalance. *Nat Mater* 15:1095–1099.
- Happel J, Brenner H (1965) *Low Reynolds Number Hydrodynamics: With Special Applications to Particulate Media* (Prentice-Hall, Englewood Cliffs, NJ).